Research Article | Vol. 10, No. 11 / 1 November 2020 / Optical Materials Express 2952
Optical Materials EXPRESS

3D printed multimode-splitters for photonic interconnects

JOHNNY MOUGHAMES,[1,2] XAVIER PORTE,[1,2,*] LAURENT LARGER,[1] MAXIME JACQUOT,[1] MUAMER KADIC,[1] AND DANIEL BRUNNER[1]

[1] Institut FEMTO-ST, Université Bourgogne Franche-Comté CNRS UMR 6174, Besançon, France
[2] Equally contributing authors
[*] javier.porte@femto-st.fr

Abstract: Photonic waveguides are promising candidates for implementing parallel, ultra-fast and ultra-low latency interconnects. Such interconnects are an important technological asset for example for next generation optical routing, on and intra-chip optical communication, and for parallel photonic neural networks. We have recently demonstrated dense optical integration of multi-mode optical interconnects based on 3D additive manufacturing using two-photon-polymerization. The basis of such interconnects are 3D optical splitters, and here we characterize their performance against their splitting ratio, geometry, and conditions of the direct laser writing. Optical losses and splitting uniformity of 1 to 4, 1 to 9 and 1 to 16 splitters are evaluated at 632 nm. We find that, both, the uniformity of splitting ratios as well as the overall losses depend on the separation between the output waveguides as well as on the hatching distance (surface quality) of the 3D printing process.

1. Introduction

Optical splitters are a fundamental component in the photonic toolbox. Splitting and combining optical waves is the indispensable ingredient of any interferometer, of delivering optical fiber-communication signals to various receivers, of linear programmable integrated photonics circuits [1] as well as of quantum-optical experiments [2]. Optical splitters are part of almost every free-space, fiber optic as well as integrated photonic system.

The device which potentially makes most heavy usage of optical splitting and combining is the optical interconnect [3], in which numerous input channels are connected to a typically comparable number of output channels. The fundamental appeal is exploiting the parallelism of photonics which promises to significantly reduce energy dissipation and latency, and therefore to mitigate some of the most disturbing limitations often encountered with electronic interconnects. Ignoring losses, an optical interconnect physically encodes a unitary connection or routing matrix, and the number of required optical mixers is proportional to the square of channels to be connected. Integration using 2D lithography, such as commonly the case in silicon-photonics, does therefore not scale in size [1,4,5] and current realizations are limited to around 10 input and output channels [6].

Recently, we have demonstrated how such optical splitters can be integrated in 3D [7]. Noteworthy, in 3D the integration of photonic interconnects or unitary vector-matrix multipliers is scalable in size. We realized connection topologies for efficient signal distribution using fractal-branching as well as spatial-filtering according to Haar-filters, and both were motivated by enabling fully parallel and scalable photonic neural networks. Integration is based on 3D additive fabrication via two-photon polymerization, which by now has been established as a flexible and robust photonic fabrication platform. It is a prolific approach for realizing free-form [8] and transformation [9] optical components, volume holograms [10], point-to-point photonic wire-bonding between optical components [8] and integrated photonic circuits in general [7,11].

#402974 https://doi.org/10.1364/OME.402974
Journal © 2020 Received 16 Jul 2020; revised 6 Sep 2020; accepted 16 Sep 2020; published 22 Oct 2020

Optical Materials EXPRESS

Our 3D waveguides have been fabricated with a commercial Nanoscribe system. They are free-standing with a polymer-core without cladding, and our waveguides with a refractive index of $n_0 \approx 1.54$ [12] (index contrast $\Delta n \approx 0.5$) support around 20 optical modes. We study branching from a single input into 4, 9 or 16 output ports and find considerably different intensity distribution between the individual output waveguides for the different splitting topologies. As most relevant parameters we identified the spacing between the regular array of output ports as well as the hatching distance, i.e. spacing between the neighboring writing voxels.

2. Design and fabrication

We realized splitters linking the single input to 4 (2×2), 9 (3×3) or 16 (4×4) output waveguides arranged in a square array with lattice distance D_0, and their design principle (cf. Figure 1(a-c)) facilitates horizontal multiplexing into large arrays as well as vertical stacking into layers based on fractal geometries [7]. At the bifurcation point the single input waveguide morphs into the numerous output waveguides, and the transition from the common input to the individual output ports is according to a sin-function. Vertical stacking into fractal, scale-free branching arrangements connects an input waveguide to an exponentially increasing number of output

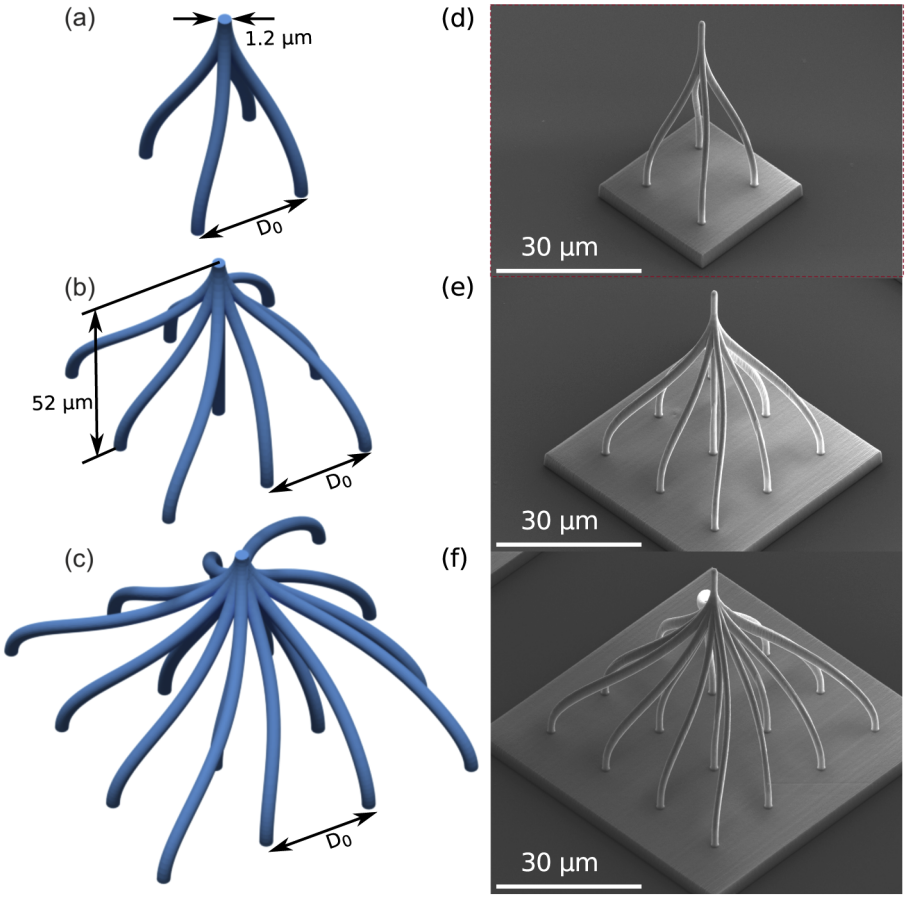

Fig. 1. Optical splitters with different numbers of output ports spaced with distance D_0 were investigated. The height of each structure was kept constant at 52 µm, the waveguides' diameter is ~1.2 µm. Their design and SEM micrographs are respectively depicted in: (a),(d) for 2×2; (b),(e) for 3×3; (c),(f) for 4×4.

Optical Materials EXPRESS

waveguides [7]. This makes very efficient use of the circuit's volume for applications depending on high connectivity, as for example often the case in fully connected layers in the final stages of deep neural networks. The shape of our splitters exhibits chirality in order to avoid un-intentionally intersecting waveguides inside the tightly packed volume. All geometric details are defined in the supplemental information of [7].

Our splitters were fabricated with a commercial 3D direct-laser writing system from Nanoscribe GmbH (Photonic Professional GT). A negative tone photoresist "Ip-Dip" was dropped on a fused silica glass substrate (25x25x0.7 mm^3) and was photo-polymerized via two-photon absorption with a λ = 780 nm femtosecond pulsed laser, focused by a 63X, (1.4 NA) microscope objective. We explored the impact of laser writing power P and the hatching distance h as well as waveguide separation D_0 at the output ports, which in turn modifies the angle at which the individual waveguides diverge at their branching points. The structures were printed in consecutive horizontal layers, superimposed in the vertical direction. The vertical distance between consecutive slices is 0.3 µm. All waveguides had a diameter of $\sim$ 1.2 µm and were written using the scanning mode based on a goniometric mirror with a constant scanning speed on the sample's surface (10 mm/s). After the writing process, samples were immersed in a PGMEA (1-methoxy-2-propanol acetate) solution for 20 minutes to remove the unexposed photoresist. Structural properties such as surface roughness of the resulting waveguides were visualized with a scanning electron microscope (SEM, Thermofisher APREO S, 5 kV, 45°), and Fig. 1(d-f) shows SEM micrographs of splitters written with P =10.4 mW.

Arrays of polymer 3D optical splitters are robust from a mechanical point of view and survive to post-printing clean-up process without a problem [7]. However, individual free-standing splitters like those depicted in Fig. 1(d-f) do not always survive the fabrication process, mostly due to insufficient adhesion to the substrate resulting in unsticking by capillary forces arising during the evaporation of the developer and rinsing with liquids. We enhanced the sturdiness of our structures by placing them on a thin, 1 µm high polymer pedestal fabricated during the same printing process. The thin plateaus resulted in the desired mechanical stability without causing a measurable influence upon the optical propagation properties. The approximated fabrication times for the different types of splitters are: 10 seconds for 2×2 splitters, 20 seconds for 3×3 splitters and 40 seconds for 4×4 splitters.

3. Structural characterization

The average writing power P directly impacts on the degree of polymerization [13,14] and the writing voxel's size. Hatching distance h, i.e. the spacing between neighbouring writing voxels, influences the polymerized material's homogeneity as well as surface roughness. They both therefore are important parameters as material inhomogeneity and surface roughness cause scattering and hence (i) induce energy transfer between different propagating modes and (ii) potentially increase optical losses. We scan two writing powers $P = \{10.4, 11.2\}$ mW and two hatching distances $h = \{0.1, 0.2\}$ µm. For our range of writing powers, the printed voxels have height and width of $\sim$ 1.2 µm and $\sim$ 0.6 µm, respectively. Mechanical stability is the reason behind the relatively small writing power range we evaluated, as for P<10.4 mW splitters were typically not stable or deformed, while P>11.2 mW regularly resulted in burning (micro explosion) of the monomer due to overexposure.

Figure 2 gives a schematic illustration of the 3D printing process and the hatching distance's impact upon the final surface quality. A pre-defined shape, in our case the optical splitter (c.f. Fig. 2(a)), is approximated through the accumulation of cigar-shaped writing voxels. The quality of this approximation is mostly governed by (i) the writing voxel's size, and (ii) by the spacing between the individual writing voxels, i.e. hatching distance h. We experimentally characterized the size of writing voxels at our writing conditions and obtained a height of 1.12 µm (1.17 µm) and diameter of 0.63 µm (0.64 µm) for a writing laser power of 10.4 mW (P =11.2 mW). The

Optical Materials EXPRESS

writing voxel's geometry therefore has impact upon the waveguides' crossection, an effect which furthermore depends on the local orientation of a waveguide relative to the writing voxel's symmetry axis. The possibility to generate 3D isotropic voxels is therefore an interesting strategy for improving homogeneity of such waveguides [15].

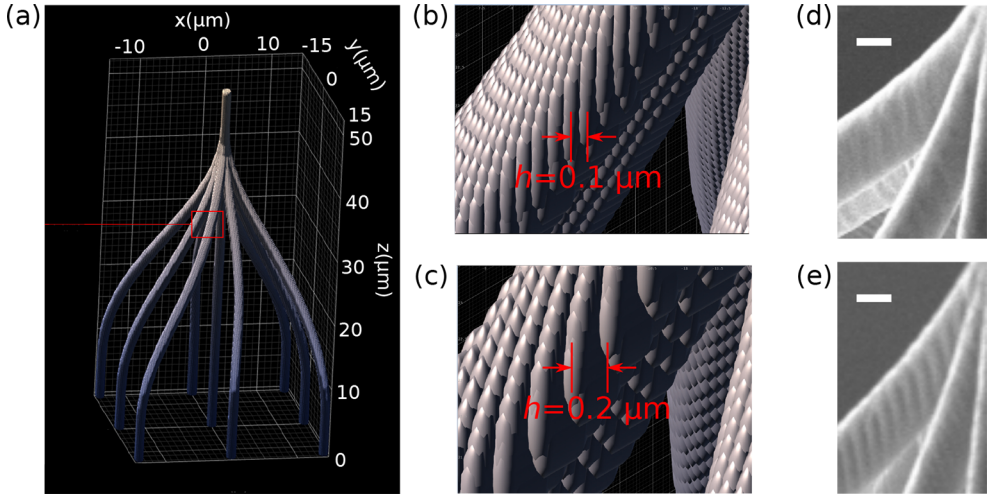

Fig. 2. The writing process of our splitters (a) (here a 3×3 splitter with $D_0 = 14$ μm) is based on the accumulation of cigar-shaped writing voxels. The defined target-shape can be approximated with different resolution, mostly determined by the hatching distance h, i.e. the spacing between the writing voxels. (b,c) illustrate the effect of writing voxels spaced with $h = 0.1$ μm and $h = 0.2$ μm, respectively, showing a zoom into the red-region of (a). SEM micrographs illustrating the waveguide's surface roughness resulting from hatching distances $h = 0.1$ μm, (d), and $h = 0.2$ μm, (e). The white scale bar inside the SEM micrographs corresponds to 1 μm.

The impact of hatching distance h can be appreciated based on an illustration considering the minimal writing voxel dimension with 0.2 μm diameter and 0.5 μm height, and for approximating our target shape with $h = 0.1$ μm (cf. Fig. 2(b)) and $h = 0.2$ μm (cf. Fig. 2(c)). The resulting surfaces are undulated by a periodic structure of a period and amplitude depending on height h, and the nature of the undulation depends on the particular surface normal relative to the writing voxel's central axis. However, diffusion during the writing process additionally smoothens the resulting surfaces, and already decreasing the hatching distance from $h = 0.2$ μm (cf. Fig. 2(b)) to $h = 0.1$ μm (cf. Fig. 2(a)) results in significantly smoother interfaces. Besides the larger surface roughness for the bigger hatching distance, one can also identify a qualitative change: printing with $h = 0.2$ μm causes a clear modulation of the surface profile with a period close to the hatching distance. This periodic impact is significantly less pronounced when printing with $h = 0.1$ μm, which indicates that other processes start to dominate. In many 3D printing scenarios, such as for mechanical meta-materials, a hatching distance of $h = 0.2$ μm is considered adequate [16,17]. However, surface roughness even on a sub-nanometer scale [18], in particular for periodic undulations [19] influences optical propagation, which suggests that hatching distance h is of major importance for 3D printing optical waveguides.

4. Optical characterization

We optically characterized the 3D-printed polymer splitters at 632 nm, and the optical characterization setup is schematically depicted in Fig. 3. The single mode Gaussian output of a fiber-pigtailed laser diode was collimated with MO_1 (Olympus PLN10X) and focused onto

Optical Materials EXPRESS

the waveguides' input facets by MO_2, a 50X microscope objective with NA = 0.8 (Olympus MPLFLN50x). The polarization was set to circular by a linear polarizer and a λ/4 waveplate (Pol and λ/4 in Fig. 3). The FWHM of the focal spot (1.3 μm) corresponds to ~ 90% of the input waveguide's diameter (≃ 1.2 μm). The splitters' optical output was collected by MO_3, a 10X microscope objective with NA=0.30 (Olympus LMPLN10XIR), and imaging using a achromatic lens (Thorlabs AC254-100-B-ML) with 100 mm focal length resulted in an optical magnification of 5.6 on the transmission camera CAM_T. The sample's input side was imaged in reflection onto reflection camera CAM_R using a 100 mm focal length achromatic lens (Thorlabs AC254-100-B-ML), resulting in a magnification of 27.8. We used identical CMOS cameras (iDS U3-3482LE, pixel size 2.2 μm) for CAM_T and CAM_R. A red LED (635 nm) creates a broad field of incoherent illumination for overall monitoring of the sample, whose position was precisely controlled with a piezo system (Thorlabs 3-Axis Nanomax MAX311D/M). We intentionally refrained from using the optical output characteristics of each splitter as alignment criteria. Instead, we aligned each splitter relative to the injection-laser focal point by maximizing the back-reflection of the input waveguide's top-facet using the reflection camera (CAM_R). This created reproducible optical injection conditions, ensuring that we characterized each splitter's generic optical properties.

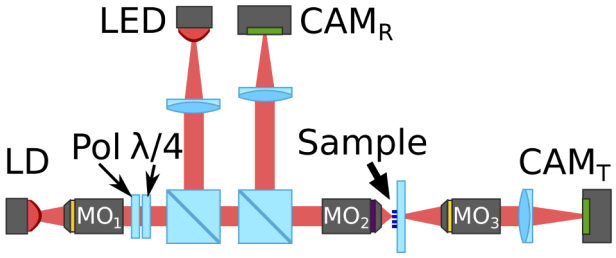

Fig. 3. Experimental setup for optical characterization, only illustrating the relevant optical components. A 635 nm LED was used as broad field illumination source for coarse positioning of the sample with a piezo nano-stage (not illustrated). A fiber coupled laser diode (LD) with 632 nm was used to measure the optical transmission of each splitter with circular polarization, which was controlled via a linear polarizer (Pol) and a $\lambda/4$ waveplate. Two CMOS cameras respectively imaged a splitter's output (CAM_T) and the reflection from the top facet of its input waveguide (CAM_R).

The intensity of the individual output waveguides as well as our transmission reference was calculated by integrating a $\simeq 4 \times 4$ μm^2 area around each output waveguide. This area is slightly larger than the waveguides' diameter, which was necessary to compensate for inaccuracies in automatically determining each output waveguide's position. However, we ensured that this larger area did not influence our characterization: manual and more accurate definition of each output waveguides' position on a test-sample allowed integrating 4 times smaller areas, and results did not differ significantly from the automatized characterization. We obtained our reference intensity by focusing the optical injection on top of the glass substrate at an area without any polymer waveguides or pedestals, and total losses were calculated by summing the optical intensity of all output waveguides normalized to this reference intensity. Total losses therefore include injection, propagation and splitting losses. Previously, we measured 2.7 dB injection and ≈20 dB/mm propagation losses for waveguides with 1.2 μm diameter [7].

5. Results

Total optical losses as well as the heterogeneity at the splitters' output ports were our primary concern. In our previous work [7] we found a quite heterogeneous intensity distribution across

Optical Materials EXPRESS

the output ports of a 3×3 splitter, which we attributed to (i) the multimode waveguides, and (ii) to a non-optimized geometry of the bifurcations. Generally, one would desire an adiabatic transition from the single to the 'bundle' of waveguides, here we therefore modify the speed at which this transition takes place by printing splitters with a range of $D_0 \in [10, 12, \ldots, 18, 20]$ µm while keeping their total height constant at 52 µm. Our injection spot is a single mode Gaussian, and transferring optical intensity to higher orders relies on material heterogeneity as well as scattering at the rough and periodically undulated waveguide surface. We therefore expect surface roughness, i.e. hatching distance h, to impact upon total losses as well as the intensity distribution across the output ports.

5.1. Total losses

Figure 4 depicts total losses for 2×2 splitters in (a,d), for 3×3 splitters in (b,e) and for 4×4 splitters in (c,f), with hatching distance $h = 0.1$ µm as blue and $h = 0.2$ µm as red data. The left column (a-c) correspond to splitters written with $P = 10.4$ mW, the right column (d-f) to $P = 11.2$ mW. The general trend indicates that total losses increase with separation D_0, with the strongest impact upon the 4×4 splitter for which the total losses change from $\sim$ 5dB to $\sim$ 11dB. There is an exception for the 2×2 splitters written with $h = 0.1$ µm where we find no impact of D_0 for $P = 10.4$ mW and even a slight reduction of losses for larger D_0 for $P = 11.2$ mW. An additional general finding is the very small relevance of writing power P, and we can conclude that this parameter is mostly relevant for the mechanical integrity of such high aspect ratio photonic structures.

The transition from the single input to the bundle of output waveguides is the slowest, hence most adiabatic for the smallest output waveguide separation $D_0 = 10$ µm. Yet, lowest losses were obtained for $D_0 = 12$ µm... 14 µm, in particular for the 3×3 and 4×4 splitters, which implies that the transition from the input waveguide to the bundle of output waveguides sensitively depends on the global geometry. This comes at no surprise as at any location waveguides support more than 20 modes; at the bifurcation points the number of supported modes is significantly larger. The principle at work for creating coupling is therefore comparable to the one employed in the multi-mode interference unit [20]. We evaluate this analogy by comparing the losses obtained when only considering the optical intensity contained inside the central 2×2 output array for the 4×4 splitters, and data are the blue and red triangles in Fig. 4(c,f) for $h = 0.1$ µm and $h = 0.2$ µm, respectively. Particular for $D_0 = 12$ µm ... 14 µm results differ significantly from the 2×2 splitter data shown in Fig. 4(a,d), and the presence of a 4×4 splitter's outer ring of waveguides clearly influences the field transferred from the single input its central 2×2 array. Furthermore, this discrepancy is amplified by increasing hatching distance h to 0.2 µm, which indicates that scattering at the waveguides' sidewalls influences coupling and the details of multi-mode interference inside the splitter's bifurcation section.

5.2. Intensity distribution

In Fig. 5 we show the experimentally obtained relative intensity distribution for symmetry groups contained within the different splitters, and the particular structures are highlighted in black inside the inset of each panel. All splitters were printed with $P = 10.4$ mW, and data for the 3×3 splitters are given in the left column (cf. Figure 5(a-c)), data for the 4×4 splitter in the right column (cf. Figure 5(d-f)). Data for $P = 11.2$ mW perfectly agrees with the shown results and is therefore not shown. Equally, we do not show data for the 2×2 splitters since these exhibit perfect symmetry and each output waveguide received a similar intensity on average. Transmission efficiencies given in Fig. 5 correspond to the integrated efficiency obtained for the output waveguides contained inside a particular group.

The main difference between both splitters is the presence (3×3) or absence (4×4) of a straight connection between the input and the output waveguides, also compare Fig. 1(b) to

Optical Materials EXPRESS

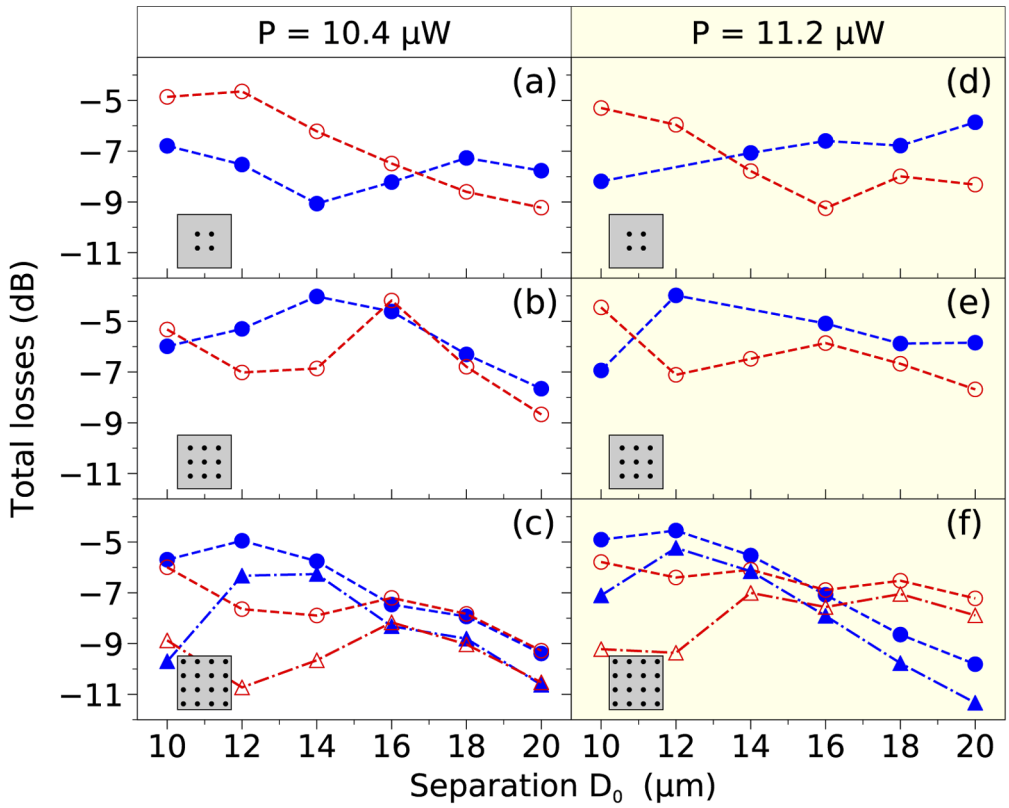

Fig. 4. Optical losses as a function of the separation between neighboring outputs D_0 and for hatching distances h = 0.1 μm and h = 0.2 μm as blue and red data, respectively. Panels respectively depict the total losses of (a,d) 2 × 2 splitters, (b,e) 3 × 3 splitters and (c,f) 4 × 4 splitters. Data in panels (a-c) correspond to splitters written with P =10.4 mW and in panels (d-f) to splitters written with P =11.2 mW. Data with triangle symbols in panels (c,f) corresponds to the central 2 × 2-array of the 4 × 4-splitter. Comparison to (a) shows that these do not agree with the 2 × 2 splitter, demonstrating that adding additional output ports influences the splitting ratios of the previous ports as well.

Fig. 1(c) for a visualization. Figure 5(a) shows that this straight connection features the majority (∼ 70%) of the 3 × 3 splitter's optical output for the smoother waveguides obtained with h = 0.1 μm and a large D_0, or for the rougher waveguides obtained with h = 0.2 μm for a small D_0. A heuristic explanation for the first case can be given quite intuitively: for smooth side-walls there is less energy transfer from the single mode injection to higher order modes, and consequently most of the injection power traverses the splitter ending up inside the 3 × 3 splitter's central output. As a direct consequence we find that the waveguides located at the sides of the 3 × 3 output waveguide array (cf. Fig. 5(b)) exhibit an almost perfectly inverted behaviour. Finally, waveguides at the 4 corners (cf. Fig. 5(c)) are hardly influenced by the surface roughness.

We find that for the 4 × 4 splitters (cf. Fig. 5(d)) the relative intensity transmitted to the central 2 × 2 array quickly reaches its maximum for around $D_0 \approx 14$ μm, where it remains at ∼ 90% for all larger D_0. There is a certain impact of h, and the relative intensity of this central sub-group of waveguides unsurprisingly reaches its maximum faster for the smoother waveguides. As before, we find that this behaviour is almost perfectly inverted by the central waveguides in the second ring (cf. Figure 5(e)), however please note that here the intensity was obtained by integrating 8

Optical Materials EXPRESS

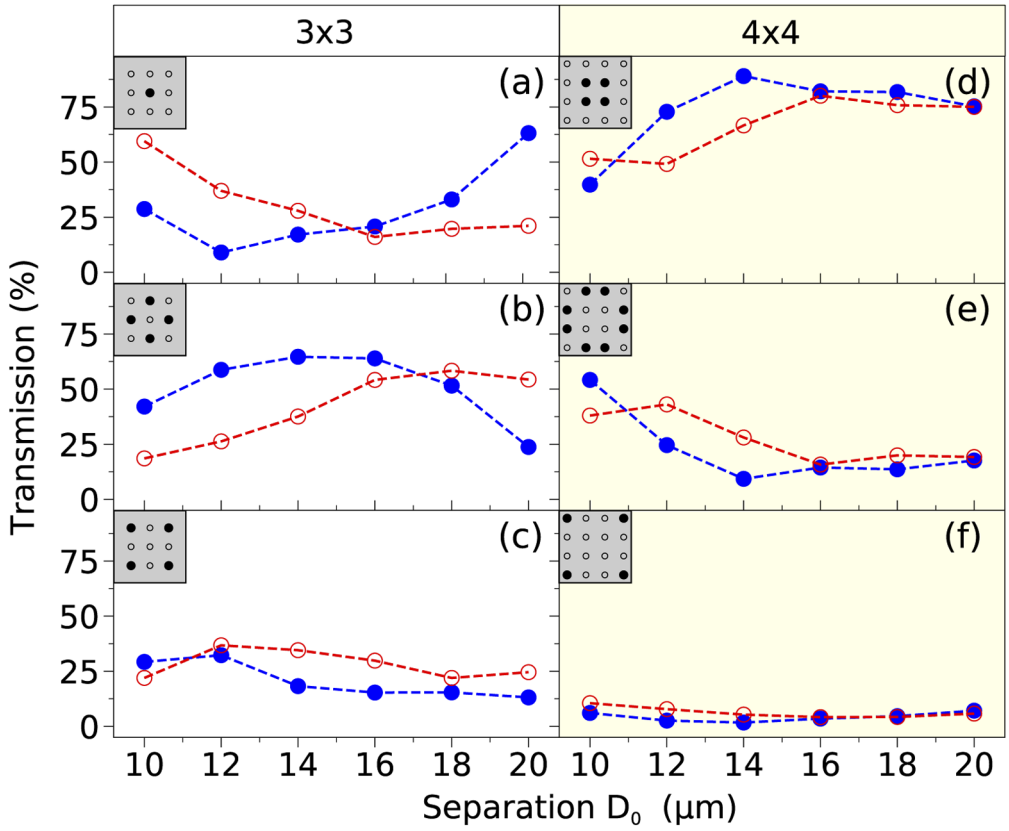

Fig. 5. Experimentally measured transmission ratios as a function of the separation between outputs. Panels respectively depict the fraction of transmission of (a,d) centers, (b,e) faces and (c,f) corners. Data from splitters with hatching distances of 0.1 and 0.2 are respectively plotted in blue and red. Data in panels (a,b,c) correspond to 3x3 splitters and in panels (d,e,f) to 4x4 splitters, both written with laser power p =10.4 mW.

output waveguides. As before, the final group of waveguides (cf. Fig. 5(f)) is hardly influenced by the surface roughness.

6. Conclusions

We characterized the optical properties of 2 photon polymerization 3D printed free standing, free standing 1 to 4, 1 to 9 and 1 to 16 waveguide splitters in detail. Such structures are relevant for a scalable and high density integration of optical interconnect [7]. We found that the optical writing power strongly influences the overall mechanical integrity of our splitters, while its impact upon the overall optical properties was rather small. The hatching distance h and the separation between output waveguides D_0, on the other hand, has a non-trivial influence. Depending on the topology, a smaller h (generally creating waveguides with smoother sidewalls) even results in higher losses.

Our results suggest that by adjusting surface roughness, i.e. hatching distance h, and distance D_0 one can to a certain degree homogenize the output of the individual splitters. This works best for the 3×3 splitters, were for h = 0.1 μm and D_0 = 14 μm the 5 waveguides arranged in a cross (see insets of Fig. 5(a,b)) exhibit an almost identical transmission ratio of ~ 15%. The most even

Optical Materials EXPRESS

optical output intensity distribution was unsurprisingly found for the symmetric 2×2 splitters. Combined with the strongly dominating central output of the 3×3 splitters, this demonstrates the importance of output waveguide arrangements for achieving symmetric output intensity distributions. For higher connectivity one should therefore employ arrangements omitting a straight central waveguide and connections to output ports arranged at $\leq 2D_0$ from the centre. Besides for the square 2×2 of a 1 to 4 splitter, this can be achieved with pentagon-arrangement for a 1 to 5 splitter, for a hexagon-arrangement for a 1 to 6 splitter, and so on.

Future version of such 3D splitters could achieve more deterministic splitting ratios be enabling single mode propagation to and from the bifurcation points, while mixing can then carefully be designed following the principles of the multi mode interference coupler [20] in the bifurcation section. Finally, detailed numerical simulations truthfully reproducing the impact of the waveguides' surface undulations are required.

Funding

H2020 Excellent Science (Marie Sklodowska-Curie 713694 (MULTIPLY).); Volkswagen Foundation (NeuroQNet I&II); Agence Nationale de la Recherche (ANR-15-IDEX-03, ANR-17-EURE-0002).

Acknowledgments

The authors acknowledge the support of the Region Bourgogne Franche-Comté. This work was supported by the EUR EIPHI program (Contract No. ANR-17-EURE- 0002), by the Volkwagen Foundation (NeuroQNet I&II), by the French Investissements d'Avenir program, project ISITE-BFC (contract ANR-15-IDEX-03) and partly by the French RENATECH network and its FEMTO-ST MIMENTO technological facility. X.P. has received funding from the European Union's Horizon 2020 research and innovation program under the Marie Sklodowska-Curie grant agreement No 713694 (MULTIPLY).

Disclosures

The authors declare no conflicts of interest.

References

1. D. A. B. Miller, "Perfect optics with imperfect components," Optica **2**(8), 747 (2015).
2. J. Cariñe, G. Cañas, P. Skrzypczyk, I. Šupić, N. Guerrero, T. Garcia, L. Pereira, M. A. S. Prosser, G. B. Xavier, A. Delgado, S. P. Walborn, D. Cavalcanti, and G. Lima, "Multi-core fiber integrated multi-port beam splitters for quantum information processing," Optica **7**(5), 542 (2020).
3. H. Lee, X. Gu, and D. Psaltis, "Volume holographic interconnections with maximal capacity and minimal cross talk," J. Appl. Phys. **65**(6), 2191–2194 (1989).
4. J. Capmany, I. Gasulla, and D. Pérez, "Microwave photonics: The programmable processor," Nat. Photonics **10**(1), 6–8 (2016).
5. J. Wang, H. Shen, L. Fan, R. Wu, B. Niu, L. T. Varghese, Y. Xuan, D. E. Leaird, X. Wang, F. Gan, A. M. Weiner, and M. Qi, "Reconfigurable radio-frequency arbitrary waveforms synthesized in a silicon photonic chip," Nat. Commun. **6**(1), 5957 (2015).
6. Y. Shen, N. C. Harris, S. Skirlo, M. Prabhu, T. Baehr-Jones, M. Hochberg, X. Sun, S. Zhao, H. Larochelle, D. Englund, and M. Soljacic, "Deep Learning with Coherent Nanophotonic Circuits," Nat. Photonics **11**(7), 441–446 (2017).
7. J. Moughames, X. Porte, M. Thiel, G. Ulliac, L. Larger, M. Jacquot, M. Kadic, and D. Brunner, "Three-dimensional waveguide interconnects for scalable integration of photonic neural networks," Optica **7**(6), 640 (2020).
8. P. I. Dietrich, M. Blaicher, I. Reuter, M. Billah, T. Hoose, A. Hofmann, C. Caer, R. Dangel, B. Offrein, U. Troppenz, M. Moehrle, W. Freude, and C. Koos, "In situ 3D nanoprinting of free-form coupling elements for hybrid photonic integration," Nat. Photonics **12**(4), 241–247 (2018).
9. M. Kadic, G. Dupont, T.-M. Chang, S. Guenneau, and S. Enoch, "Curved trajectories on transformed metal surfaces: Beam-splitter, invisibility carpet and black hole for surface plasmon polaritons," Photonics Nanostructures-Fundamentals Appl. **9**(4), 302–307 (2011).

Optical Materials EXPRESS

10. N. U. Dinc, J. Lim, E. Kakkava, C. Moser, and D. Psaltis, "Computer generated optical volume elements by additive manufacturing," Nanophotonics **9**(13), 4173–4181 (2020).
11. J. Pyo, J. T. Kim, J. Lee, J. Yoo, and J. H. Je, "3D Printed Nanophotonic Waveguides," Adv. Opt. Mater. **4**(8), 1190–1195 (2016).
12. S. Dottermusch, D. Busko, M. Langenhorst, U. W. Paetzold, and B. S. Richards, "Exposure-dependent refractive index of Nanoscribe IP-Dip photoresist layers," Opt. Lett. **44**(1), 29 (2019).
13. L. J. Jiang, Y. S. Zhou, W. Xiong, Y. Gao, X. Huang, L. Jiang, T. Baldacchini, J.-F. Silvain, and Y. F. Lu, "Two-photon polymerization: investigation of chemical and mechanical properties of resins using Raman microspectroscopy," Opt. Lett. **39**(10), 3034 (2014).
14. A. Žukauskas, I. Matulaitiene, D. Paipulas, G. Niaura, M. Malinauskas, and R. Gadonas, "Tuning the refractive index in 3D direct laser writing lithography: Towards GRIN microoptics," Laser Photonics Rev. **9**(6), 706–712 (2015).
15. W. Chu, Y. Tan, P. Wang, J. Xu, W. Li, J. Qi, and Y. Cheng, "Centimeter-Height 3D Printing with Femtosecond Laser Two-Photon Polymerization," Adv. Mater. Technol. **3**(5), 1700396 (2018).
16. L. Yang, A. Münchinger, M. Kadic, V. Hahn, F. Mayer, E. Blasco, C. Barner-Kowollik, and M. Wegener, "On the schwarzschild effect in 3D two-photon laser lithography," Adv. Opt. Mater. **7**(22), 1901040 (2019).
17. T. Frenzel, J. Köpfler, E. Jung, M. Kadic, and M. Wegener, "Ultrasound experiments on acoustical activity in chiral mechanical metamaterials," Nat. Commun. **10**(1), 3384 (2019).
18. X. Ji, F. A. S. Barbosa, S. P. Roberts, A. Dutt, J. Cardenas, Y. Okawachi, A. Bryant, A. L. Gaeta, and M. Lipson, "Ultra-low-loss on-chip resonators with sub-milliwatt parametric oscillation threshold," Optica **4**(6), 619 (2017).
19. A. Nicolet, F. Zolla, Y. O. Agha, and S. Guenneau, "Leaky modes in twisted microstructured optical fibers," Waves in Random and Complex Media **17**(4), 559–570 (2007).
20. L. Soldano and E. Pennings, "Optical multi-mode interference devices based on self-imaging: principles and applications," J. Lightwave Technol. **13**(4), 615–627 (1995).